J. Plasma Phys. (2015), *vol.* 81, 495810502 © Cambridge University Press 2015
doi:10.1017/S0022377815000604

Complex astrophysical experiments relating to jets, solar loops, and water ice dusty plasma

P. M. Bellan[1],†, X. Zhai[1], K. B. Chai[1] and B. N. Ha[1]

[1]California Institute of Technology, Pasadena, CA 91125, USA

(Received 17 April 2015; revised 8 May 2015; accepted 12 May 2015)

Recent results of three astrophysically relevant experiments at Caltech are summarized. In the first experiment magnetohydrodynamically driven plasma jets simulate astrophysical jets that undergo a kink instability. Lateral acceleration of the kinking jet spawns a Rayleigh–Taylor instability, which in turn spawns a magnetic reconnection. Particle heating and a burst of waves are observed in association with the reconnection. The second experiment uses a slightly different setup to produce an expanding arched plasma loop which is similar to a solar corona loop. It is shown that the plasma in this loop results from jets originating from the electrodes. The possibility of a transition from slow to fast expansion as a result of the expanding loop breaking free of an externally imposed strapping magnetic field is investigated. The third and completely different experiment creates a weakly ionized plasma with liquid nitrogen cooled electrodes. Water vapour injected into this plasma forms water ice grains that in general are ellipsoidal and not spheroidal. The water ice grains can become quite long (up to several hundred microns) and self-organize so that they are evenly spaced and vertically aligned.

1. Introduction

This paper presents an overview of astrophysically relevant experimental plasma research conducted at Caltech during the past several years and updates the previous overview given in Bellan *et al.* (2010). Three different experiments will be discussed, two closely related to each other, and the third very different. The two related experiments use pulsed power methods to create magnetohydrodynamic (MHD)-governed plasmas having topology and dynamics similar to astrophysical jets and solar corona loops while the third experiment involves creation of a dusty plasma where the dust is very cold water ice. The experiments have in common that they have the goal of discovering new phenomena rather than simply verifying some existing theoretical model. Several unexpected phenomena have been discovered and models have been developed to explain these phenomena. The experiments are not claimed to be exact scale replicas of actual astrophysical situations, but rather their purpose is to generate new insights into the physics governing astrophysical phenomena. The results should be quite relevant to astrophysical and solar situations because plasma physics in general and MHD in particular have no intrinsic scale. The experiments will be discussed in the following order: (i) astrophysical jet, (ii) solar corona loop, and (iii) water ice dusty plasma.

† Email address for correspondence: pbellan@caltech.edu

https://doi.org/10.1017/S0022377815000604 Published online by Cambridge University Press

2. Astrophysical jet experiment

In much of plasma physics, especially fusion research, analysis of phenomena typically starts off with the assumption that an equilibrium exists and then attention is focussed on analysing the structure and properties of this equilibrium. In particular, MHD configurations are typically assumed to satisfy the equilibrium equation

$$\boldsymbol{J} \times \boldsymbol{B} = \nabla P. \tag{2.1}$$

Analysis of this equation leads to the Bennett pinch relation (Bennett 1934) and the Grad–Shafranov equation (Grad & Rubin 1958; Shafranov 1966).

Magnetic field lines are often sketched to characterize the essence of some proposed situation and the evolution of the system is often interpreted as a slow evolution from one (2.1) equilibrium state to another. Because current density is a function of magnetic field via Ampere's law $\boldsymbol{J} = \mu_0^{-1}\nabla \times \boldsymbol{B}$, sketching magnetic field lines when discussing solutions to (2.1) is tantamount to assuming that for any assumed magnetic field $\boldsymbol{B}(\boldsymbol{x})$ it is always possible to find a pressure profile $P(\boldsymbol{x})$ satisfying (2.1).

A critical result of the research reported here is the realization that in fact it is not possible to find a pressure profile $P(\boldsymbol{x})$ that satisfies (2.1) for an arbitrary assumed magnetic field $\boldsymbol{B}(\boldsymbol{x})$. Thus, when one sketches a magnetic field, typically no equilibrium exists for the sketched field. The reason why equilibria do not exist for arbitrary magnetic field configurations is that the curl of the right-hand side of (2.1) is always zero by virtue of mathematical identity, whereas there is no reason why the curl of $\boldsymbol{J} \times \boldsymbol{B}$ must be zero. In fact, the curl of $\boldsymbol{J} \times \boldsymbol{B}$ is generally finite and is zero only for certain special situations having a high degree of symmetry. If the curls of the two sides of (2.1) are not equal, then (2.1) is not a valid equation. The terms $\boldsymbol{J} \times \boldsymbol{B}$ and $-\nabla P$ are force densities, so their curl corresponds to a torque. The $-\nabla P$ force is conservative and so has no torque, but typically $\boldsymbol{J} \times \boldsymbol{B}$ is non-conservative and so has an associated torque. The $\boldsymbol{J} \times \boldsymbol{B} \neq \nabla P$ situation implies that unbalanced forces exist having an associated torque. These forces drive flows and the associated finite torque means that these flows will have vorticity and a circulation.

The astrophysical jet and solar corona loop experiments have unbalanced forces of this sort driving plasma flows. Combined experimental and theoretical investigations have provided insight into the evolution and topology of these flows. The experiments have a distinct sequence which has been studied in detail and is now well understood. The current focus of attention is on effects that are more complicated than the basic flow mechanism.

The vacuum chamber and electrodes for the astrophysical jet experiment are shown in figure 1. The vacuum chamber is very large compared to the jet to simulate infinite space. The experimental setup consists of (i) a coil that generates a dipole poloidal magnetic field, (ii) a disk electrode, (iii) a coplanar annulus electrode, (iv) holes in both electrodes that act as gas nozzles, (v) fast gas puff valves, and (vi) a high-energy capacitor bank that is discharged across the two electrodes. Initialization of the experiment consists of energizing the coil to produce the dipole magnetic field (time scale about 5 ms) followed by puffing in gas through eight holes in the disk and eight holes in the annulus (time scale about 1 ms). These two initialization steps are sketched in figure 2.

After the initialization described above, the high-energy capacitor bank is connected across the two electrodes by an ignitron switch; the ignitron switching time is about 1 μs and the ignitron is capable of handling high voltage (∼10 kV) and high current (∼100 kA). Application of the high voltage initiates the sequence summarized in figure 3. This sequence consists of the following.

https://doi.org/10.1017/S0022377815000604 Published online by Cambridge University Press

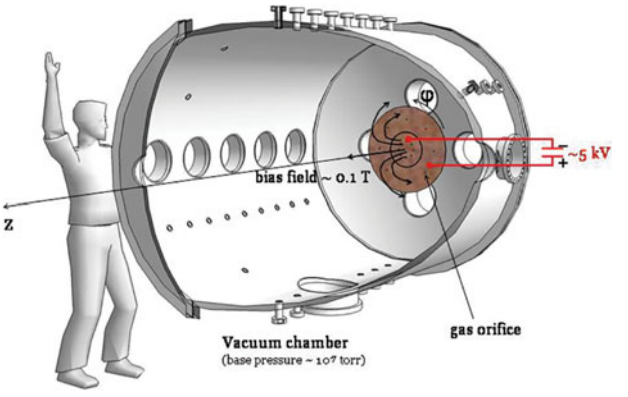


FIGURE 1. Layout of electrodes and power supply for astrophysical jet experiment. Curved black lines with arrows are dipole magnetic field produced by coil located behind electrodes.

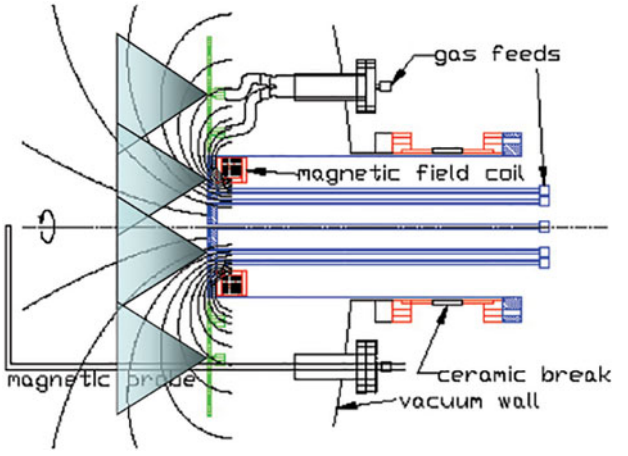


FIGURE 2. Initialization: the dipole field is first established (characteristic time about 5 ms) and then fast valves open to puff in gas from eight orifices in the disk and eight orifices in the annulus (characteristic time about 1 ms).

(i) The high voltage breaks down the gas to form a very low density plasma. A small electric current flows along poloidal magnetic field lines going from the disk to the annulus; these field lines link a gas nozzle on the disk to a gas nozzle on the annulus.

(ii) A very fast plasma jet flows from the disk nozzle to the annulus nozzle to form a plasma-filled flux tube spanning the respective disk and annulus nozzles while following the poloidal field produced by the coil. Because the disk and annulus each have eight evenly spaced holes there are eight such arched plasma-filled flux tubes. Together they have the morphology of the eight legs of a spider (figure 3*a*). The time for the spider legs to form is about 1 μs.

(iii) The inner parts of the spider legs mutually attract because they are close to each other and have parallel electric currents; at the same time the major radius of each spider leg increases because of the hoop force acting on a curved current

https://doi.org/10.1017/S0022377815000604 Published online by Cambridge University Press

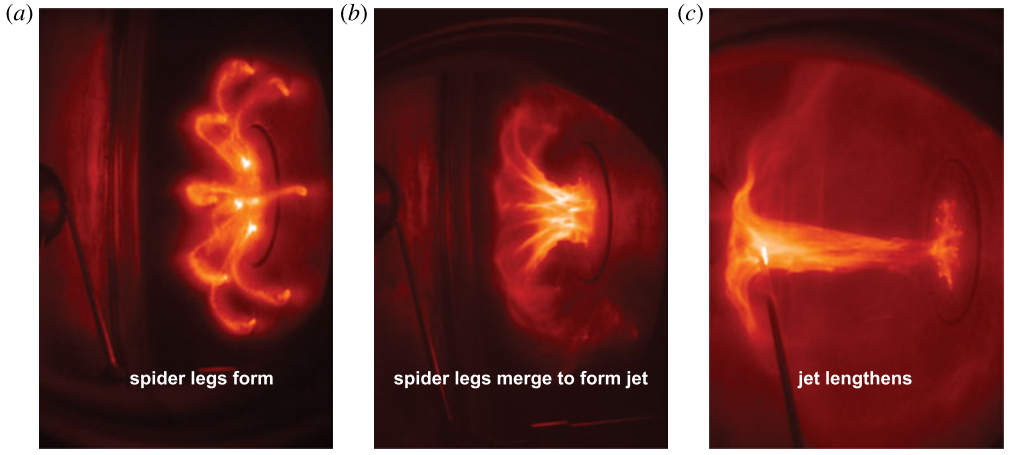


FIGURE 3. Jet sequence: (*a*) spider legs form, (*b*) inner parts of legs merge to form jet, (*c*) jet lengthens.

(figure 3*b*). This major radius increase can be interpreted by any of the following equivalent descriptions: the pressure of the toroidal field produced by the poloidal current flowing in the spider legs acts to inflate the spider legs, the $J_r B_\phi$ axial force accelerates the spider legs in the z direction, or the return current in the capacitor bank repels the oppositely directed current in the spider legs.

(iv) Once the inner spider legs have completely merged, the configuration has a mushroom-like topology where the jet is the stalk. The jet length increases with a 10–60 km s^{-1} velocity with the precise value depending on the current, the density, and the gas species (figure 3*c*). The model explaining the jet velocity involves a two-stage argument (Bellan 2006). The jet velocity results from axial acceleration caused by the axial component of $\boldsymbol{J} \times \boldsymbol{B}$ in combination with the axial component of $-\nabla P$, where the pressure P is first determined by a local radial force balance. The radial force balance depends on axial position – there is a higher pressure on-axis near the electrodes than far from the electrodes. The resulting on-axis pressure gradient provides the on-axis axial force that accelerates the jet on-axis. Acceleration on-axis via a pressure gradient is essential because $J_r B_\phi - J_\phi B_r$, the axial component of the magnetic force, vanishes on-axis since both J_r and B_r vanish on the axis. Local radial force balance results in an on-axis pressure $P \sim B_\phi^2/2\mu_0 \sim \mu_0 I^2/a^2(z)$, where I is the axial current and $a(z)$ is the jet radius. On the axis, a Bernoulli relation exists such that $P + \rho U_z^2 = \text{const}$. Substituting for P in this Bernoulli relation using the local radial force balance gives a jet velocity $U_z(z) \sim \mu_0 I/(2\pi a(0)\sqrt{\mu_0 \rho(z)})$. This scaling has been verified experimentally (Kumar & Bellan 2009) by measuring the velocity for different values of current and also for different gases to determine the dependence on ρ. A three-dimensional time-dependent numerical simulation (Zhai *et al.* 2014) using the MHD equations shows good quantitative agreement with this model and with the experiment. Figure 4 shows side-view synthetic images constructed from the results of the numerical simulation compared to actual side-view photographs of the jet. Because the plasma is optically thin, a camera image is the integral of the emission along the line of sight. The local emission at each point on the line of sight scales

https://doi.org/10.1017/S0022377815000604 Published online by Cambridge University Press

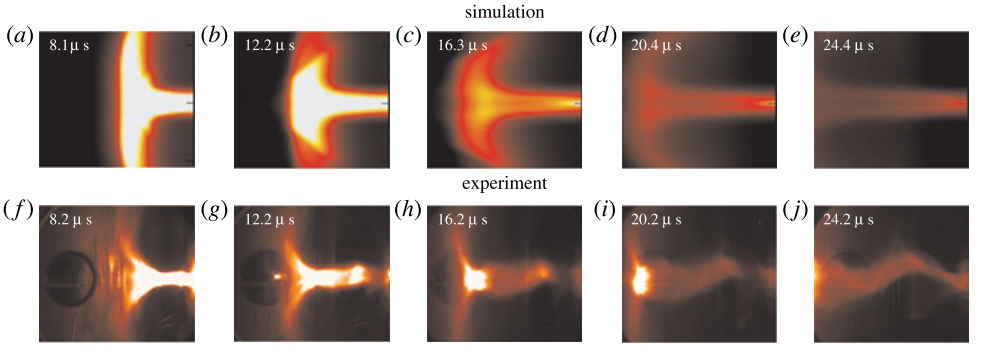


FIGURE 4. (*a–e*) show synthetic images constructed from 3D numerical simulation. (*f–j*) show photographs of an actual plasma. Figure from Zhai *et al.* (2014).

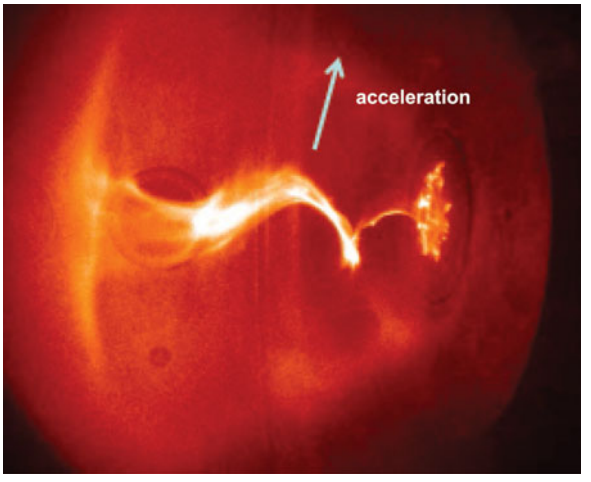


FIGURE 5. Jet kinks when it attains critical length corresponding to $q = 1$. Arrow shows local direction of acceleration as kink grows exponentially.

as $n_e n_i \sim n_e^2$ because atomic line emission is a binary process involving a free electron impacting an ion. The synthetic images in figure 4(*a–e*) are constructed from line averages along the line of sight of the numerically calculated n_e^2 while (*f–j*) shows actual photographs. The close match between the top and bottom images indicates that the simulation accurately models the shape and velocity of the actual plasma. The photographs of the real plasma and the simulated photographs differ significantly only for the 24.2 μs frame, where the real plasma has started to kink. The simulation does not capture the kink, presumably because small deviations from azimuthal symmetry in the actual plasma have not been programmed into the numerical simulation.

(v) When the jet attains a critical length, it undergoes an ideal MHD kink instability as shown in the bottom right frame of figure 4 and in more detail in figure 5. The kink onset is in agreement (Hsu & Bellan 2003) with the $q = 1$ limit of a straight cylindrical tokamak where $q = 2\pi a B_z/(L B_\phi)$ with a being the jet radius and L being the jet length. When the jet is formed, L is small so q starts out large, but,

https://doi.org/10.1017/S0022377815000604 Published online by Cambridge University Press

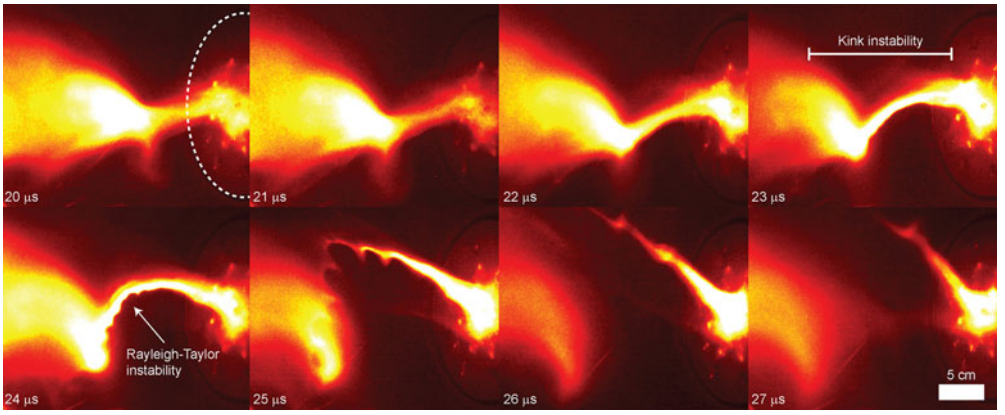


FIGURE 6. Kink develops from 20 to 23 μs and then at 24 μs RT ripples develop on inboard side of curved jet. The ripples grow by a factor of three in just 1 μs as seen in 24 μs frame. Figure is from Moser & Bellan (2012).

as the jet lengthens, q decreases until it reaches unity and the kink destabilizes. Typically, kink onset occurs when the jet length is 20–40 cm. The kink grows very fast with characteristic growth time much less than the jet propagation time. From the point of view of the kink, the jet may as well be standing still.

(vi) Because the kink causes the jet to develop an exponentially growing corkscrew shape, an observer attached to the jet would experience an exponentially growing lateral displacement and an associated exponentially growing lateral velocity. This increasing velocity corresponds to a lateral acceleration as indicated by the arrow in figure 5. The acceleration is very large, about 10^9–10^{10} m s^{-2}, and provides the conditions for development of an even faster secondary instability (Moser & Bellan 2012). This secondary instability is a Rayleigh–Taylor (RT) instability, which occurs because the fast lateral acceleration would appear as an effective gravity to an observer in the jet frame. Since the jet density greatly exceeds the density just outside the jet, the dense jet with adjacent near-vacuum in the presence of the large effective gravity is effectively a heavy fluid on top of a light fluid, which is the situation required for a RT instability. As seen in the 24 and 25 μs frames of figure 6, the heavy jet on top of the light external near-vacuum develops a RT instability. The RT instability is much faster than the kink instability and so from the point of view of the RT instability the kink instability is standing still.

(vii) The RT instability has a much shorter time scale and a much shorter length scale than the kink instability (see figure 6). The RT instability produces the following effects, which are now under investigation.

(*a*) Because the RT instability occurs on the 'down' side of the jet where up and down refer to the sense of the local gravity, the RT interchange reduces the jet cross-sectional area at axial locations where the RT instability appears concave to an external observer. This reduction of the jet cross-sectional area increases the current density in the jet. If this localized choking of the jet reduces the effective jet radius to being less than the ion skin depth, ideal MHD becomes inappropriate and a collisionless reconnection based on two-fluid concepts occurs (Moser & Bellan 2012). Evidence of such magnetic

https://doi.org/10.1017/S0022377815000604 Published online by Cambridge University Press

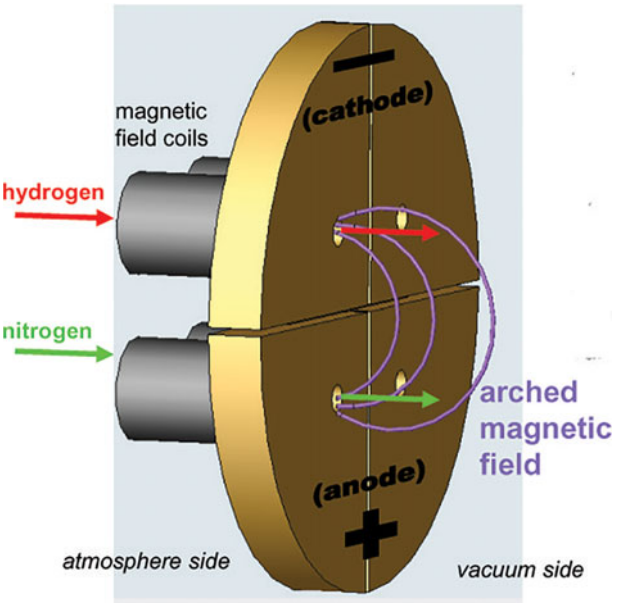


FIGURE 7. Solar corona loop setup with different gases (hydrogen and nitrogen) injected at the two footpoints to test the hypothesis that jets emanate from each footpoint to populate the loop with plasma. Figure from Stenson & Bellan (2008).

reconnection is observed when heavy gases such as argon are used but not when hydrogen, a light gas, is used. This difference is attributed to the ion skin depth of hydrogen being much smaller than that of argon so for a given density reducing the jet radius will access the argon ion skin depth limit before accessing the hydrogen ion skin depth limit. It is observed that the RT instability is much stronger in argon than in hydrogen and hydrogen jets often do not manifest obvious RT instability (Moser & Bellan 2012).

(*b*) A burst of extreme ultraviolet (EUV) radiation is observed coincident with the RT instability (Moser & Bellan 2012). High-speed movies of the EUV radiation indicate that the source of this radiation is situated at the RT instability (Chai & Bellan 2013*a*).

(*c*) Spectroscopic measurements of atomic lines indicate that higher ionization states exist when the RT instability occurs.

(*d*) Capacitive probe measurements show a burst of high-frequency waves (Moser & Bellan 2012). The frequency of these waves is in the whistler regime and wave magnetic field measurements underway tentatively identify these waves as being whistler waves on the basis of oblique whistler wave magnetic polarization properties discussed in Bellan (2014).

The working hypothesis is that the RT instability locally destroys the jet forcing a fast collisionless reconnection with associated change in topology. The reconnection has a large transient electric field that accelerates electrons. When these energetic electrons collide with argon ions, the ions are excited to a higher energy atomic state and EUV radiation is emitted.

https://doi.org/10.1017/S0022377815000604 Published online by Cambridge University Press

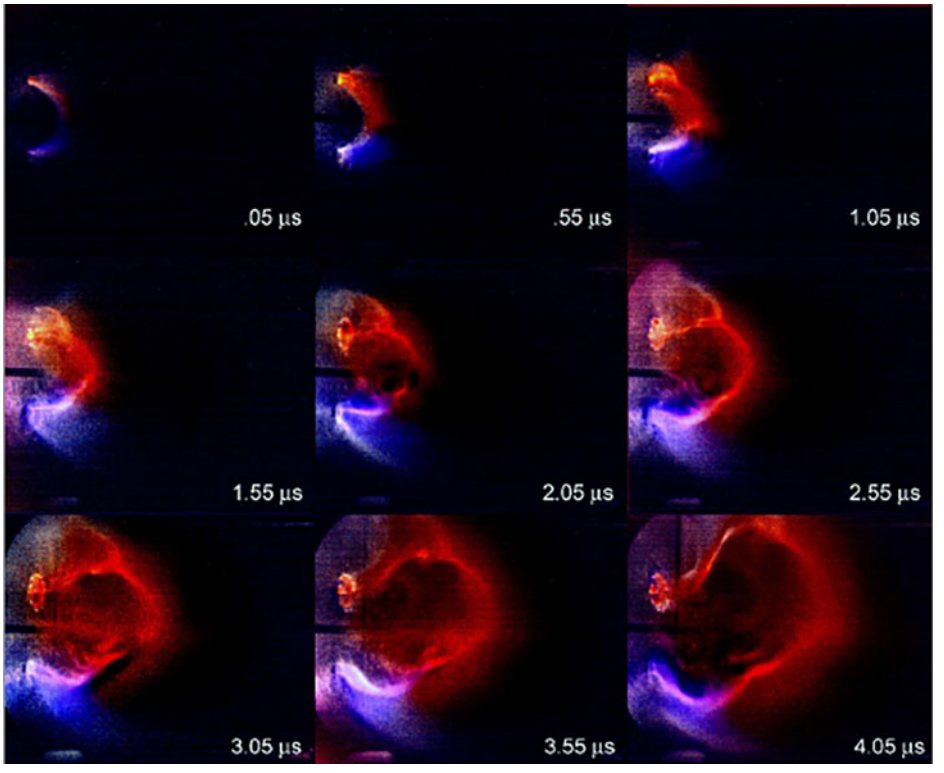


FIGURE 8. Composite image showing hydrogen jet (red) originating from top electrode butting up against nitrogen jet (blue) originating from bottom electrode. Together, the two jets populate the expanding loop with plasma. Figure from Stenson & Bellan (2008).

3. Solar corona loop experiment

Technology similar to the astrophysical jet experiment is used to create arched plasma loops having the geometry of solar corona loops. The setup for this experiment is sketched in figure 7. These loops expand as a result of the hoop force caused by the curvature of the path followed by the electric current flowing along these arched loops. These loops are essentially a single spider leg of the astrophysical jet experiment described in § 2. The direction of jet flow is independent of the sign of the electric current flowing along the jet because the forces scale as the square of this current. The jet flows from regions where the current channel radius is small to where the current channel radius is large. Because the current channel radius is smallest at the footpoints (electrodes), flows are expected to originate at both electrodes. This implies that there should be two jets, one from each electrode, and these jets should flow towards each other. To demonstrate that there are indeed two such jets, hydrogen was injected into one footpoint and nitrogen was injected into the other (Stenson & Bellan 2008, 2012). The result was a hydrogen jet originating from the footpoint where the hydrogen gas was injected and a nitrogen jet originated from the footpoint where the nitrogen gas was injected. The jet velocities are much larger than the thermal velocity of the neutral gases. Plasma in the arched flux tube was then composed of the hydrogen and nitrogen jets,each originating from its respective footpoint.

https://doi.org/10.1017/S0022377815000604 Published online by Cambridge University Press

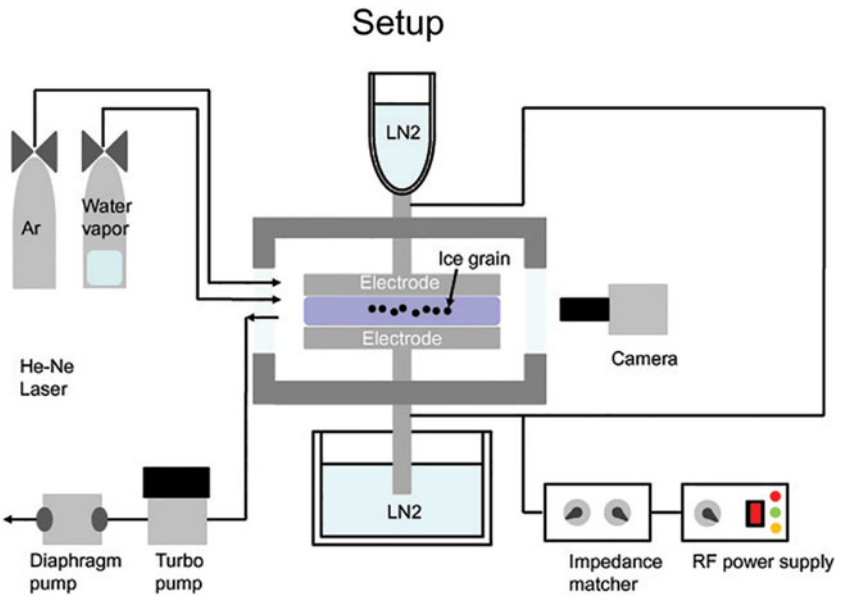


FIGURE 9. Setup for water ice dusty plasma experiment. A weakly ionized plasma is produced using a parallel-plate rf discharge. The electrodes have cold fingers that are immersed in liquid nitrogen. Controlled amounts of water vapour are introduced into the system. The water vapour spontaneously forms water ice grains – this happens only if there is plasma and the background gas is cooled by the cold fingers immersed in liquid nitrogen.

This was demonstrated by putting optical filters in front of the camera so as to be able to distinguish the hydrogen plasma from the nitrogen plasma. A colour-coded superposition of the images of the hydrogen and nitrogen jets is shown in figure 8, which reveals that the plasma loop is indeed composed of the two jets colliding with each other head-on. Because the loop major radius expands in proportion to the rate at which the jets lengthen (Stenson & Bellan 2012), the two jets never pass through each other.

An experiment is underway to investigate the torus instability proposed by Kliem & Török (2006) as a mechanism explaining the slow build-up of energy followed by sudden release commonly observed in solar eruptions. The torus instability involves adding an external 'strapping' magnetic field (Hansen & Bellan 2001) that interacts with the current flowing in the loop so that the force acting on the loop is $\boldsymbol{J}_{loop} \times (\boldsymbol{B}_{loop} + \boldsymbol{B}_{ext})$, where $\boldsymbol{B}_{loop}$ is the self-field of the current $\boldsymbol{J}_{loop}$ flowing along the loop and $\boldsymbol{B}_{ext}$ is the external strapping field. By arranging for the strapping field to have a rapid spatial decay above a certain altitude, an initially strapped down loop having an increasing current will gradually rise to the altitude where the strapping field has a rapid spatial decay with altitude. When the loop breaches this critical altitude, the loop is no longer strapped down and begins a fast expansion. There will consequently be a transition from slow to fast expansion, i.e. an eruption. Preliminary measurements have indicated that this process occurs when a strapping field with a suitably arranged spatial decay is imposed.

https://doi.org/10.1017/S0022377815000604 Published online by Cambridge University Press

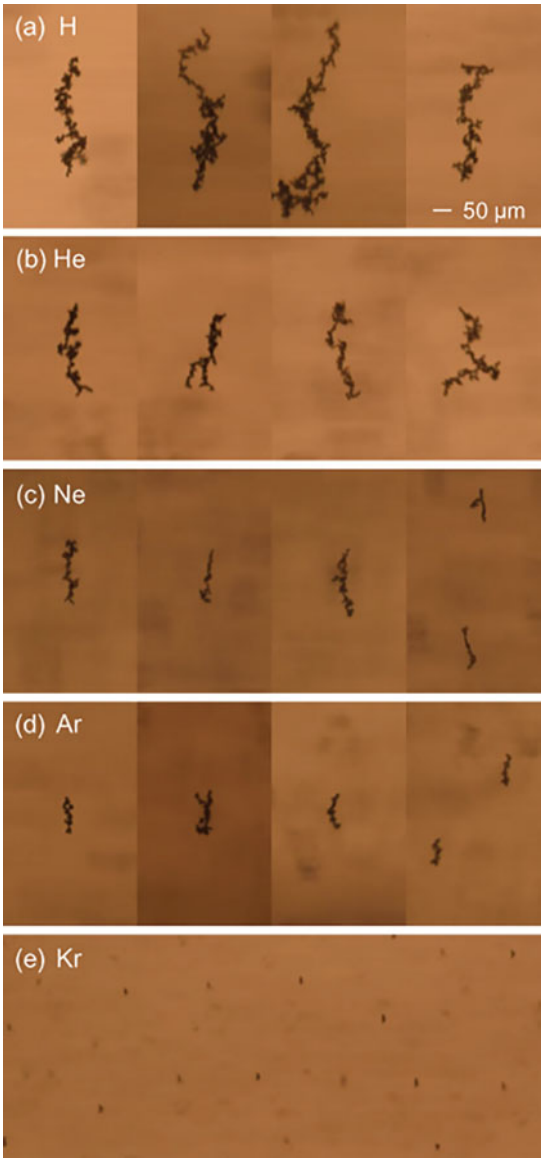


FIGURE 10. Ice grains formed with different background gases. The ice grains are larger and more non-spherical for lower mass background gases. This is believed due to greater deflection occurring when a water molecule collides with a heavy gas compared to a light gas. Figure from Chai & Bellan (2015).

4. Water ice dusty plasma experiment

The dusty plasma experiment uses an electrode cooling concept based on Shimizu *et al.* (2010), who first observed formation of water ice in a plasma. However, the method for injecting water differs because water is directly injected rather than created in the plasma by chemical bonding of oxygen and a hydrogen isotope. As sketched in figure 9, electrodes in a conventional rf gas discharge are attached to cold fingers immersed in liquid nitrogen. The cold fingers pass through electrically

https://doi.org/10.1017/S0022377815000604 Published online by Cambridge University Press

isolated, vacuum-tight seals as the liquid nitrogen is at atmospheric pressure whereas the electrodes are in vacuum. The liquid nitrogen cools the electrodes to very low temperatures. A small controlled amount of water vapour is injected into the vacuum chamber. When there is the combination of weakly ionized plasma, water vapour, and cooling, water ice grains spontaneously form and grow (Chai & Bellan 2013*b*, 2015). The size and shape of the ice grains depend on ambient conditions such as plasma density, rf power, and gas density. The ice grains are non-spherical at low pressures, self-organize into a lattice pattern, and are co-aligned. Ice grains formed with various background gases are shown in figure 10. The length-to-width ratio is as high as 5:1 and the ice grains can have lengths as large as several hundred microns. Ice grains have also been produced using methanol and acetone instead of water (Chai & Bellan 2015).

Acknowledgements

This material is based upon work supported by the US Department of Energy Office of Science, Office of Fusion Energy Sciences under award numbers DE-FG02-04ER54755 and DE-SC0010471, by the National Science Foundation under award number 1059519, and by the Air Force Office of Scientific Research under award number FA9550-11-1-0184.

REFERENCES

BELLAN, P. M. 2006 *Fundamentals of Plasma Physics*. pp. 334–338. Cambridge University Press.

BELLAN, P. M. 2014 Circular polarization of obliquely propagating whistler wave magnetic field. *Phys. Plasmas* **20**, 082113.

BELLAN, P. M., KUMAR, D., STENSON, E. V., TRIPATHI, S. K. P., YUN, G. S. & MOSER, A. L. 2010 Laboratory simulations of astrophysical jets and solar coronal loops: new results. In *Proceedings of International Symposium on Plasmas in the Laboratory and in the Universe: Interactions, Patterns and Turbulence, Como, Italy, 1–4 December 2009* (ed. G. Bertin, F. DeLuca, G. Lodato, R. Pozzoli & M. Rome), AIP Conference Proceedings, vol. 1242, pp. 156–163. AIP.

BENNETT, W. H. 1934 Magnetically self-focussing streams. *Phys. Rev.* **45**, 890–897.

CHAI, K. B. & BELLAN, P. M. 2013*a* Extreme ultra-violet movie camera for imaging microsecond time scale magnetic reconnection. *Rev. Sci. Instrum.* **84** (12), 123504.

CHAI, K. B. & BELLAN, P. M. 2013*b* Spontaneous formation of nonspherical water ice grains in a plasma environment. *Geophys. Res. Lett.* **40** (23), 6258–6263.

CHAI, K. B. & BELLAN, P. M. 2015 Formation and alignment of elongated, fractal-like water–ice grains in extremely cold, weakly ionized plasma. *Astrophys. J.* **802** (1), 112.

GRAD, H. & RUBIN, H. 1958 MHD equilibrium in an axisymmetric toroid. In *Proc. 2nd UN Conf. on the Peaceful Uses of Atomic Energy*, vol. 31, p. 190. IAEA.

HANSEN, J. F. & BELLAN, P. M. 2001 Experimental demonstration of how strapping fields can inhibit solar prominence eruptions. *Astrophys. J.* **563**, L183–L186; Part 2.

HSU, S. C. & BELLAN, P. M. 2003 Experimental identification of the kink instability as a poloidal flux amplification mechanism for coaxial gun spheromak formation. *Phys. Rev. Lett.* **90**, 215002.

KLIEM, B. & TÖRÖK, T. 2006 Torus instability. *Phys. Rev. Lett.* **96** (25), 255002.

KUMAR, D. & BELLAN, P. M. 2009 Nonequilibrium Alfvénic plasma jets associated with spheromak formation. *Phys. Rev. Lett.* **103** (10), 105003.

MOSER, A. L. & BELLAN, P. M. 2012 Magnetic reconnection from a multiscale instability cascade. *Nature* **482**, 379–381.

SHAFRANOV, V. D. 1966 Plasma equilibrium in a magnetic field. In *Reviews of Plasma Physics*, vol. 2, p. 103. Consultants Bureau.

https://doi.org/10.1017/S0022377815000604 Published online by Cambridge University Press

SHIMIZU, S., KLUMOV, B., SHIMIZU, T., ROTHERMEL, H., HAVNES, O., THOMAS, H. M. & MORFILL, G. E. 2010 Synthesis of water ice particles in a plasma chamber. *J. Geophys. Res. Atmos.* **115**, D18205.

STENSON, E. V. & BELLAN, P. M. 2008 Dual-species plasmas illustrate MHD flows. *IEEE Trans. Plasma Sci.* **36** (4), 1206–1207.

STENSON, E. V. & BELLAN, P. M. 2012 Magnetically driven flows in arched plasma structures. *Phys. Rev. Lett.* **109** (7), 075001.

ZHAI, X., LI, H., BELLAN, P. M. & LI, S. T. 2014 Three-dimensional MHD simulation of the Caltech plasma jet experiment: first results. *Astrophys. J.* **791** (1), 40.

https://doi.org/10.1017/S0022377815000604 Published online by Cambridge University Press